

¹ Wind veer and speed in turbulent Ekman flow part I:
² scaling analysis and universal velocity profile model

³ Cedrick Ansorge¹ and Hauke Wurps^{2,3}

⁴
⁵ Submitted March 27, 2025

⁶ **Abstract**

⁷ The profiles of wind speed and direction in turbulent Ekman flow are formulated
⁸ based on asymptotic theory and data from direct numerical simulation. The profile
⁹ of the streamwise component, considered in a wall-stress-aligned reference frame,
¹⁰ follows the classical viscous, logarithmic and wake scaling. In the outer layer, the
¹¹ velocity component profiles can be described by an Ekman-spiral with adapted
¹² boundary conditions that result in a reduction of the spiral-like rotation. The
¹³ span-wise component poses a conceptual challenge to the channel-flow analogy
¹⁴ in the context of asymptotic matching; it exhibits a mixed scaling in the surface
¹⁵ layer, but follows outer scaling for most of the outer layer. Viscous stress scales
¹⁶ universally across the boundary layer in inner units while the total stress be-
¹⁷ comes universal as a function of outer height~~the outer height, commonly denoted~~
¹⁸ as z^- . This implies a mixed scaling for the turbulent stress and eddy viscosity
¹⁹ across the inner layer and convergence to a universal-scaling as function of the
²⁰ outer height across the outer layer for increasing scale separation vide Reynolds
²¹ numbers, i.e. for increasing Reynolds number. The extrapolation to these scaling
²² to atmospheric scale separation is confirmed via large-eddy simulation in part II
²³ of this manuscript.

²⁴ **Keywords** Direct Numerical Simulation · Scale Separation · Ekman Layer · Sur-
²⁵ face Layer · Hodograph

²⁶ **1 Introduction**

²⁷ The Coriolis force bends the apparent path of motion on a rotating sphere and
²⁸ establishes geostrophic equilibrium when in balance with a pressure gradient force.
²⁹ Wind veer away from the wind direction in geostrophic equilibrium is (i) due to

¹ FU Berlin, Institut für Meteorologie, Carl-Heinrich-Becker-Weg 6–10, 12165 Berlin, Germany
cedrick@posteo.de

² Carl von Ossietzky Universität Oldenburg, School of Mathematics and Science, Institute of Physics

³ ForWind - Center for Wind Energy Research, Küppersweg 70, 26129 Oldenburg, Germany

30 direct frictional effects in the very vicinity of the surface and (ii) due to turbulence
 31 which exerts indirect frictional effects; these effects cause a slow-down of the mean
 32 wind reducing the Coriolis force thus turning the wind in favor of the pressure
 33 gradient force. Not only does the veering set the frame of reference for surface
 34 layer theory, it also has effects at small and large scales from large-scale dispersion
 35 via plume spreading to cyclone spin-down (Svensson and Holtslag 2009) and on
 36 the capabilities of data assimilation and accuracy of surface flux estimates (Brown
 37 et al. 2005). From a large-scale perspective, the veering of wind across the plane-
 38 tary boundary layer determines the amount of cross-isobaric mass-flux, commonly
 39 referred to as 'Ekman pumping' (Ekman 1905), and it is thus a key factor in the
 40 life-cycle of large-scale synoptic systems. Within the atmospheric boundary layer
 41 (ABL), directional shear of the wind in the upper part of the surface layer may
 42 cause a systematic yaw for tall wind power generation devices where blades reach
 43 into the Ekman layer, i.e. that part of the boundary layer where the wind starts to
 44 turn; an exact estimate of such effects is critical in the site assessments for wind
 45 farms (Calaf et al. 2010; Mirocha et al. 2018).

46 In the planetary boundary layer, wind veer is characterized by the surface
 47 veering angle α defined as the angle between the negative surface shear stress τ_{sfc}
 48 and the geostrophic wind. Surface veering α and geostrophic drag $Z \equiv u_*/G$, where
 49 the friction velocity $u_* \equiv \sqrt{|\tau_{sfc}|/\rho}$, uniquely determine the surface drag τ_{sfc} in a
 50 turbulent Ekman flow. In any quantitative description of the surface layer, the
 51 friction velocity u_* is the dynamic scale and α defines the horizontal alignment
 52 of the frame of reference, i.e. the rotation of the surface friction with respect
 53 to the outer wind direction. Knowledge about u_* and α is thus a prerequisite
 54 for any quantitative theory of the surface layer, and Rossby and Montgomery
 55 (1935) constrained the two parameters based on integral relations in the ABL.
 56 Asymptotic similarity theory was later used by Tennekes (1973); Blackadar and
 57 Tennekes (1968), and–based on his seminal direct numerical simulations (DNS)
 58 of Ekman flow–, Spalart (1989) suggested a modification to take into account
 59 effects of low to intermediate Reynolds numbers. Later on, constants were re-
 60 evaluated with a focus on the ABL based on observations (Högström 1988, 1996)
 61 and numerical modelling (Spalart et al. 2008, 2009; Ansorge and Mellado 2014;
 62 Ansorge 2019).

63 Attempts were also undertaken to obtain profiles of the wind speed: One ap-
 64 proach is to match the inner and outer layer at a reference height as suggested by
 65 Eting (2002); Emeis (2018) (Sec. 21.10; Eq. 21.48); they choose the Prandtl-layer
 66 ~~height $z_{Prandtl}$ depth, a measure for the depth of the surface layer,~~ to match the
 67 wind speed profiles, ~~which, however,~~. However, this requires external prescription
 68 of $\alpha(z_{Prandtl})$, the veering at that height. A one-dimensional profile with constant
 69 veering is given by Emeis et al. (2007, Sec. 3; Eq. 3.1-3.19).

70 Gryning et al. (2007) present an extension of the wind-speed profile beyond the
 71 surface layer using a neutral reference profile and a stability correction; Kelly and
 72 Gryning (2010), based on a probabilistic representation of stratification, develop
 73 a model for the long-term mean wind speed in the ABL and compare this with
 74 observation at different sites; Kelly and Troen (2016) demonstrate the effect of
 75 such improved model for wind-energy applications. In consideration of the large
 76 scale separation in geophysical flow, the rotation of the wind in the surface layer is
 77 often assumed negligible, and above investigations merely focus on the wind speed;
 78 that means, the veering of the wind with height is not described and there is little

knowledge on the profile of the span-wise velocity component and the precise shape of the hodograph in the limit of a truly neutral Ekman boundary layer. A climatology of wind turning in the ABL is given by Lindvall and Svensson (2019) Klein et al. (2021) use a statistical turbulence modelling approach that yields a two-component velocity profile, but they also find that the exact representation of turning is challenging.

Ekman-layer models are roughly based on Ekman's seminal 1905 paper in combinations with additional assumptions. One option is a prescribed profile shape for eddy viscosity (Ellison (1955)), another are two-layer models of the ABL that take into account rotational effects at higher altitudes, for instance when the wind speed needs to be evaluated at heights on the order of 100 – 200 m, a particular concern when it comes to wind-power forecasting (Etling 2002; Emeis 2018; Optis et al. 2014). Despite rotational effects being considered, the formulation of these models for the outer layer and analysis of their performance primarily focuses on wind speed. Still, in 2018, Jiang et al. recognized that the outer part of the Ekman boundary layer receives less attention in comparison with the surface layer and study the neutral problem by Large-Eddy simulation (LES). They focus on the wind speed and find an extended logarithmic layer when considering the wind speed instead of the shear-aligned component, and they eventually demonstrate by means of an analytical model that this vertical extension of the logarithmic layer may be explained by a transfer of stress to the span-wise velocity component where it is assumed that the shear vector $\tau(z)$ and stress vectors $(\partial_z U, \partial_z V)$ are aligned.

More recently, Ghannam and Bou-Zeid (2021) treated the horizontally averaged momentum budget to show that departures from shear-alignment in the vicinity of the surface result in an integral of the wind veer (α_M in their notation) over the height to very high accuracy ($\int_{z_0}^H \sin \alpha_M$ in their notation; their Eq. (16)). Classic surface-layer similarity is recovered when the angle α_M does not depend on height, i.e., the wind veer is constant across the surface layer. If, however, the wind veer depends on height, the profiles of stress and mean velocities depart from the scalings implied by classic surface-layer similarity.

Turbulent Ekman flow is considered here as a conceptual model of the homogeneous, stationary ABL over a flat surface and under neutral stratification. ~~Universal profiles of the wind vector for turbulent Ekman flow not only are The description of velocity profiles for this strongly simplified problem is not only a canonical fluid-mechanical problem, but it also constitutes~~ a well-described limit for theoretical exploration or higher-order approaches taking into account possible effects of stratification, roughness or other physical complications encountered in the real geophysical system. While, on first sight, the study of such a strongly idealized case appears as an academic problem, it contains the essence of surface similarity as it is used in most atmospheric models, be it conceptual or numeric ones. More complex accounts generally refer to the homogeneous stationary problem as a base state: (i) Roughness is commonly incorporated by a linear transformation of vertical scale involving the roughness parameter z_0 and for larger roughness also a displacement height (Monin and Yaglom 1975; Jacobs and Van Boxel 1988; Högström 1988); (ii) Stability can be accounted for by a linearization around the neutrally stratified profile (Monin 1970; Monin and Yaglom 1975; Högström 1988, 1996; Sakagami et al. 2020); (iii) Non-stationarity in the pressure-gradient forc-

ing can be accounted for by a linear damped-oscillator approach around the base state(Momen and Bou-Zeid 2016); (iv) Barotropic and baroclinic effects on the velocity profile require ~~to consider~~consideration of the height-dependence of the veer and stress misalignment (Momen et al. 2018; Ghannam and Bou-Zeid 2021). Furthermore, such a solution can serve as better initial condition for numerical simulation of the flow, to minimize the length of initial transient periods, or as benchmark for turbulence closures that can be tuned to reproduce the neutral limit case.

Despite the strong simplifications implied by our choice of set-up, there is no straightforward approach to solving this well-defined problem. Large-Eddy simulation not only needs to be tuned for the surface shear stress and veering angle, but it also relies on sub-grid closures that commonly assume alignment of the turbulent stress with gradients. This pre-requisite is not fulfilled when the wind rotates with height. Esau (2004) investigated the representation of the Ekman boundary layer by dynamical subgrid closures and Zikanov et al. (2003) proposed a closure for the wind profile using a linearized representation of the eddy viscosity. Despite advances in analysis of this simplified set-up (Jiang et al. 2018), there is yet insufficient understanding for a quantitative generalization of the results to arbitrary external forcing (manifest in variation of the Reynolds number) – and indeed the fundamental questions pertaining to such relatively simple dynamics of turbulence are not reflected in the research on LES for the ABL over the past 50 years (Stoll et al. 2020).

At the same time, an increasing amount of high-quality and high-resolution data from turbulence-resolving approaches is emerging due to recent advances in high-performance computing and its application to geophysical problem sets; the geophysical range of scale separation, however, is—and it will remain so for the foreseeable future—out of reach for such simulation (Dimotakis 2005). Here, the routinely employed concept of Reynolds-number similarity can help. It postulates the existence of *fully developed turbulence* believed to occur for a sufficiently large but finite Reynolds number (Barenblatt and Goldenfeld 1995). (Already in 1998, this in fact lead Moin and Mahesh to the question *how high a Re is high enough?*) Certain statistics of fully developed turbulence, such as dissipation (Dimotakis 2005) or profiles of mean velocity (Barenblatt 1993), become independent of the Reynolds number when appropriately scaled; other statistics, such as the near-wall maximum in velocity fluctuation depend on Re (Baars and Marusic 2020) and externality of the flow may exert an impact on near-wall scaling (da Silva et al. 2014). It appears that for certain statistics in Ekman flow, fully-developed turbulence is reached with the Reynolds numbers that became possible due to an increase of computing capabilities over the past decades.

This paper exploits the robust features of mean velocity profiles from direct numerical simulation across a range of Reynolds numbers to formulate both the streamwise and span-wise components of the mean velocity vector as a function of the Reynolds number.

170 2 Problem formulation and numerical approach

171 We consider here incompressible, turbulent Ekman flow, that is, the turbulent flow
 172 over a flat rotating plate, as a physical model for the truly neutral ABL. The f-

173 plane approximation is applied such that rotation only acts on horizontal velocity
 174 components; we thus neglect, i.e. rotation acts on the horizontal components of
 175 velocity alone; rotational effects on the horizontal components vertical component
 176 of velocity and dynamical effects due to latitudinal variation of the rate of rotation
 177 are neglected.

178 2.1 Notation and governing equations

179 The dimensional velocity vector of the numerical simulations is $\underline{U} = (U_1, U_2, U_3) =$
 180 (U, V, W) over the coordinate system $Oxyz$, where an approximate alignment (plus/
 181 minus few degrees) of the direction Ox with the surface shear stress is achieved.
 182 We consider velocity profiles only, i.e. all velocities are averaged over horizontal
 183 planes and in time, that is, they correspond to an Ensemble ensemble average. The
 184 coordinate Oz points away from the wall, and Oy points in the span-wise direction
 185 normal to Oxz . For analysis of the results, we use two coordinate systems that are
 186 (i) exactly aligned with the surface shear stress

$$\underline{\tau}_{\text{sfc}} = \begin{pmatrix} \tau_x \\ \tau_y \\ \tau_z \end{pmatrix} = -\rho\nu \left(\frac{\partial U}{\partial z} \hat{e}_x + \frac{\partial V}{\partial z} \hat{e}_y \right) \quad (1a)$$

187 and labelled by an upper index α as in \underline{U}^α for the velocity vector, and (ii) the
 188 coordinate system aligned with the free-atmosphere geostrophic wind labelled by
 189 an upper index G as in \underline{U}^G . We denote the square root of the modulus of surface
 190 shear, the surface friction, by

$$u_* = \sqrt{\|\underline{\tau}_{\text{sfc}}\|} \sqrt{\frac{\|\underline{\tau}_{\text{sfc}}\|}{\rho}} \quad (1b)$$

191 and let $Z_* = G/u_*$; the surface veering angle α_* is the angle between $\underline{\tau}$ and the
 192 geostrophic wind

$$\alpha_* = \sphericalangle(\underline{G}, \underline{\tau}_{\text{sfc}}). \quad (1c)$$

193 Analogously, we denote the height-local veering of the wind $\alpha(z) = \sphericalangle(\underline{G}, \underline{U}(z))$,
 194 where $\underline{G} = (G_1, G_2, 0)$ is the geostrophic wind vector.

195 We consider the incompressible Navier–Stokes equations for the three velocity
 196 components on the f-plane in a framework that is governed by (i) geostrophic wind
 197 magnitude $G = \sqrt{G_1^2 + G_2^2}$, (ii) Coriolis parameter f (representing the angular
 198 rotation), and (iii) kinematic viscosity ν . In absence of external variability, this
 199 system converges to a statistically steady state in the sense that flow statistics
 200 do not depend on time; and this state is defined by a Reynolds number, the only
 201 non-dimensional parameter that governs the system (in Ekman flow, the ratio of
 202 Rossby and Reynolds number are not independent as $Re_D = 2A/D$). We use the
 203 geostrophic wind as velocity and the Coriolis parameter f as time scale for the
 204 non-dimensional framework. This implies the Rossby radius $A_{\text{Ro}} = G/f$ as length
 205 scale, such that one Reynolds number governing the problem reads as

$$Re_A = \frac{GA_{\text{Ro}}}{\nu}. \quad (2)$$

206 The scales used in defining Re_A are of limited relevance for description of the
 207 turbulent flow state. The turbulence scale separation in a wall-bounded flow is
 208 commonly characterized by the friction Reynolds number (Jiménez 2012):

$$\text{Re}_\tau = \frac{u_* \delta}{\nu} = \delta^+ = \frac{\text{Re}_A}{Z_*^2}, \quad (3)$$

209 where $\delta = u_*/f$ and we use a superscript '+' to denote normalization by inner tur-
 210 bulence scales (u_* , ν). The outer normalization (with respect to the boundary-layer
 211 depth δ and velocity u_*) is denoted by a superscript '-', i.e. $z^- = z/\delta$. Another
 212 common measure of scale separation is the Reynolds number

$$\text{Re}_D = \frac{GD}{\nu} \quad (4)$$

213 defined by the laminar Ekman layer thickness $D = \sqrt{2\nu/f}$.

214 The governing equations non-dimensionalized by G , f , and A_{Ro} read as

$$\frac{\partial u_i}{\partial t} = \frac{\partial \pi}{\partial x_i} - u_j \frac{\partial u_i}{\partial x_j} + \epsilon_{i2j}(u_j - g_j) + \frac{1}{\text{Re}_A} \frac{\partial^2 u_i}{\partial x_j^2} \quad (5a)$$

$$\frac{\partial u_j}{\partial x_j} = 0, \quad (5b)$$

215 where $u_i = U_i/G$ are the non-dimensional components velocity, π is non-dimen-
 216 sional pressure, $g_j = G_j/G$ are non-dimensionalized components geostrophic wind
 217 (with $g_1^2 + g_2^2 = 1$ by construction), and ϵ is the Levi–Civita tensor. These equations
 218 are solved inside a bounded cube of size $L_x \times L_y \times L_z$ with periodic boundary condi-
 219 tions in the lateral (streamwise and spanwise) directions, a no-slip–no-penetration
 220 boundary at $z = 0$, and a no-penetration, free-slip boundary at $z = L_z$.

221 2.2 Numerical simulations

222 The problem is solved numerically by tLab¹, an open-source tool-suite to simulate
 223 and analyze turbulent flows. We use here a fourth-order–five-step Runge–Kutta
 224 integration and sixth-order compact schemes for spatial derivatives in all direc-
 225 tions. The incompressibility constraint is enforced by a fractional step approach
 226 where the Poisson equation for the pressure field is solved to machine accuracy
 227 using a combined spectral/compact approach as described in Mellado and Ansorge
 228 (2012).

229 Simulations used here are shown in Tab. 1. We extend an existing set of simula-
 230 tions for $\text{Re}_A \in \{125\,000; 281\,250; 500\,000\}$ (gray shading; cf. Ansorge and Mellado
 231 2014, 2016) by new simulations at higher Reynolds numbers up to $\text{Re}_A = 1.28 \times 10^6$
 232 with a horizontal domain extent up to 3.3×10^4 viscous units. In total, this yields
 233 one order of magnitude variation in terms of the scale separation in the boundary
 234 layer.

¹ <https://github.com/turbulencia/tlab>

Table 1 Direct numerical simulation data sets used in this work. Re_A and Re_D refer to the Reynolds number defined in terms of the Rossby radius Λ and Ekman-layer thickness D respectively. L_{xy} is the domain size in the stream- and span-wise direction. The grid is given by the number of grid points in the stream-wise (N_x), span-wise (N_y) and vertical (N_z) directions respectively. The resolution in the span-wise and stream-wise directions are given as Δx^+ and Δy^+ . The grid in the vertical is stretched, and resolution at the wall is given by Δz^+ .

Re_A	Re_D	L_{xy}/Λ	$N_x \times N_y \times N_z$	Δx^+	Δy^+	$\Delta z^+ _{z=0}$
125 000	500	1.08	$2048 \times 2048 \times 192$	4.1	4.1	1.05
281 250	750	1.08	$3072 \times 3072 \times 384$	5.6	5.6	1.60
500 000	1 000	1.08	$3072 \times 6144 \times 512$	9.3	4.7	1.14
845 000	1 300	0.54	$2560 \times 5120 \times 640$	8.9	4.5	0.99
1 280 000	1 600	0.54	$3860 \times 7680 \times 960$	8.6	4.3	1.00

Table 2 DOIs and reference to the openly accessible data set at refubium repository

Re_D	DOI	Reference
500	10.17169/refubium-42505	Ansorge (2024a)
1000	10.17169/refubium-42507	Ansorge (2024b)
1300	10.17169/refubium-42508	Ansorge (2024c)
1600	10.17169/refubium-42509	Ansorge (2024d)

235 3 Scaling behavior of the flow for Re_τ up to 3000

236 The generalization of profiles to arbitrary Reynolds numbers requires sufficient
 237 scale separation in the simulations, not only to quantify the effect of the Reynolds
 238 number on low-order flow statistics, but also to assess the corresponding rate-of-
 239 change to eventually allow for an extrapolation of the findings. While the simula-
 240 tions previously available (gray shading in Tab. 1) give confidence in a first-order
 241 representation of the turbulent problem, the estimation of higher-order effects such
 242 as the dependency of the Reynolds number requires a broader scale separation that
 243 is made available by the two new simulations at increased Reynolds number (cf.
 244 Tab. 1). Data at such scale separation has been obtained previously (cf. Spalart
 245 et al. 2008, 2009), but we also need high confidence with respect to the convergence
 246 of simulation data for slow oscillations and with respect to sampling convergence,
 247 which translates to two further requirements on the data: First, data should be free
 248 of artifacts from long-term oscillations across the vertical extent of the domain—
 249 primarily, simulations should be free of effects originating from the inertial oscil-
 250 lation; this is achieved here by replacing the mean value of the three-dimensional
 251 velocity fields by the time mean over a whole inertial oscillation. Second, high
 252 accuracy is also needed in terms of the statistical convergence of averages, bulk
 253 measures and large-scale structures; this requires a domain size $L_x > \mathcal{O}(\delta_{95})$. We
 254 use here $L_x = L_y = 1.08\Lambda$ for cases with $Re \leq 1000$ and $L_x = L_y = 0.54\Lambda$ for
 255 $Re \geq 1300$ which corresponds to $L_x/\delta_{95} \approx 25$ for $Re_D = 500$ and $L_x/\delta_{95} \approx 18$ for
 256 $Re_D = 1300$.

257 Bulk parameters of the simulations are given in Tab. 3. The surface stress is
 258 characterized by u_* and α_* in relation to the geostrophic wind vector and dis-
 259 cussed in more detail as the drag law below in Sec. 4.1 (we find the expected slight
 260 decrease of u_*/G and α_* with increasing Re). The boundary-layer height estimated
 261 from the 95% stress reduction, δ_{95} , is around 0.6δ to 0.66δ . Interestingly, the in-
 262 tegrated TKE $\int_0^\delta edz$ stays constant when normalized by the friction velocity u_*

Table 3 Bulk characterization of the simulations for different Reynolds numbers Viscous Reynolds number Re , friction Reynolds number Re_τ , friction velocity u_* , surface veering angle α_* , normalized boundary layer depth δ_{95}/δ , inner normalization of vertically integrated TKE, outer normalization of vertically integrated dissipation.

Re	$\delta^+ = \text{Re}_\tau$	u_*/G	α_*	δ_{95}/δ	$f u_*^{-3} \int_0^\delta \epsilon dz$	$G^{-3} \int_0^\delta \epsilon dz$
500	479	0.0619	25.5	0.66	0.88	1.31
750	886	0.0561	21.0	0.65	0.90	1.34
1000	1403	0.0530	18.8	0.62	0.92	1.30
1300	2122	0.0501	17.9	0.59	0.85	1.24
1600	2978	0.0482	17.2	0.61	0.91	1.21

while the integrated dissipation $\int_0^\delta \epsilon dz$ exhibits inviscid scaling when normalized by the magnitude G of the geostrophic wind. (TKE and dissipation normalized as $fG^{-3} \int \epsilon dz$ and $u_*^{-3} \int \epsilon dz$, exhibit substantial dependence on Re for the variation of u_* .) This indicates that the bulk dissipation is governed by the forcing G -irrespective of Re . Changes in Re , however, affect the level and organization of turbulence, and the parameter representing this dependency is the friction velocity u_* which describes the turbulence production processes in the surface layer, in particular in the buffer layer.

Velocity profiles in inner units ($U^{\alpha+}(z^+)$, Fig. 1a) and outer units ($U^{\alpha-}(z^-)$, Fig. 1b) are in accordance with previous work (Coleman et al. 1992; Spalart et al. 2008, 2009; Ansorge and Mellado 2014; Ansorge 2019): The profiles of the shear-aligned streamwise velocity component are well-collapsed for $\text{Re}_D > 500$ below $z^- \approx 0.15$ (circles in Fig. 1a); the case with $\text{Re}_D = 500$ is only transitionally turbulent and there is no distinct inner-outer scale separation. The logarithmic law is appropriate for $50 < z^+ < 0.15 \text{Re}_\tau$, where $z^+ = \text{Re}_\tau z^-$. While the profiles $U^{\alpha+}(z^+)$ diverge between different Re beyond $z^- = 0.15$, the corresponding profiles of the velocity deficit ($U^{\alpha+}(z^-) - G_1^\alpha$) agree closely, irrespective of Re . This illustrates the inner–outer scale-duality in this external flow with inner scaling being appropriate in the inner layer and outer scaling in the outer layer. Also in the outer layer of the flow, u_* (and not the magnitude of the geostrophic wind G) governs the inviscid normalization, i.e. a scaling independent of the Reynolds-number.

No collapse is found for the profiles of spanwise velocity when considered in inner units, $V^{\alpha+}(z^+)$. When normalized in outer units, the deficit profiles of spanwise velocity $(V^{\alpha+}(z^-) - G_2^\alpha)/u_*$ agree well beyond $z^- \approx 0.3$. This is a much higher level in comparison with the streamwise component that collapses also within the overlap layer, i.e. much closer to the surface (circles in Fig. 1b). The value of $V^{\alpha+}(z^-) - G_2^\alpha$ is sensitive to the wind veering for $z \rightarrow 0$ as—for use of the shear-aligned component—it has to approach the value $-G_2^\alpha = |G| \sin \alpha \neq 0$ in view of the no-slip boundary condition. While low-Re effects appear to be present for $\mathcal{O}(\text{Re}) < 10^3$, the spanwise component converges to an Re -independent limit within the range of scale separation considered here, i.e.

$$G_2^\alpha/u_* = Z_* \sin \alpha \rightarrow \text{const. for } \text{Re} \rightarrow \infty, \quad (6)$$

which has indeed already been found by Spalart (1989), who estimates the constant from an integral relation.

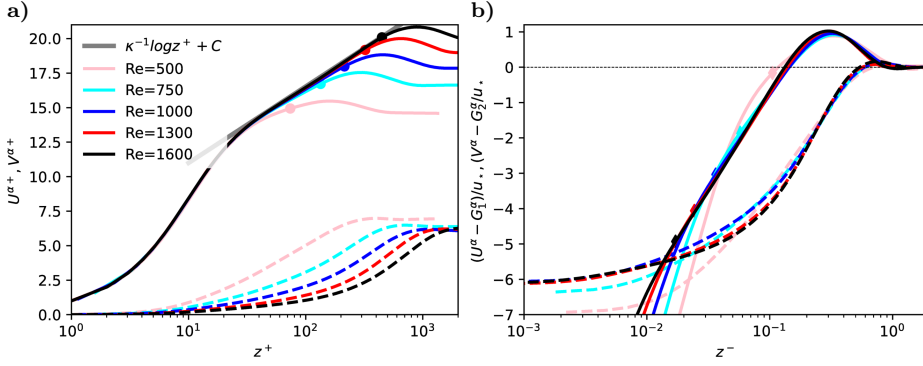


Fig. 1 a) Shear-aligned velocity profiles in inner units; circles mark the height $z^- = 0.15$; b) Shear-aligned velocity deficit in outer units; diamonds mark the grid point closest to the height $z^+ = 50$

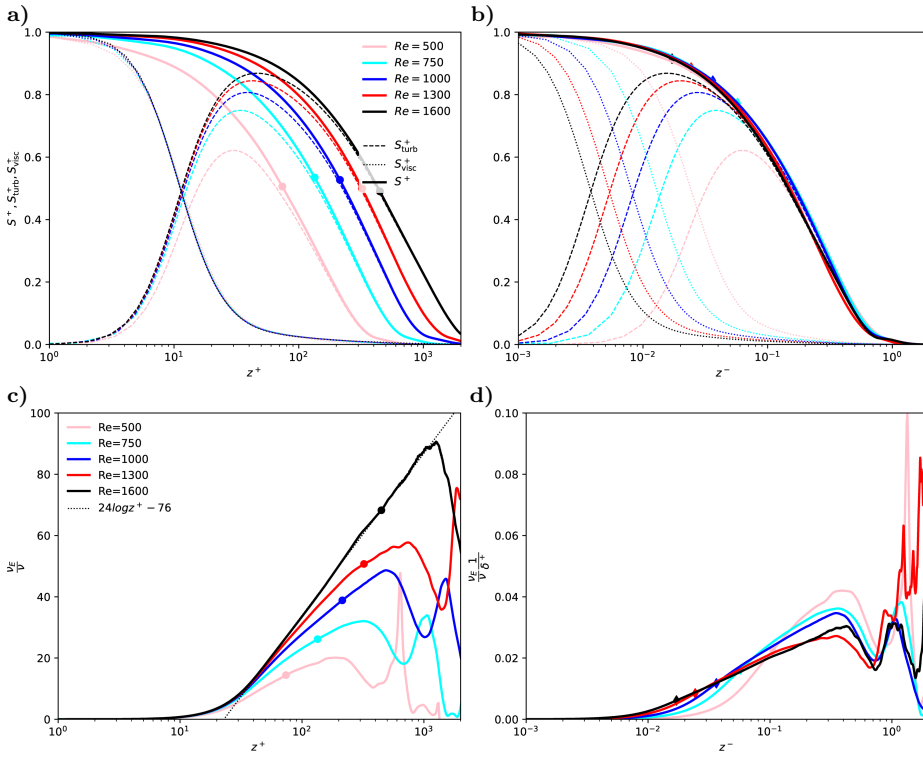


Fig. 2 a-b) Profiles of the turbulent stress S_{turb}^+ (dashed), the viscous stress S_{visc}^+ (dotted), and the total stress, $S^+ = S_{\text{visc}}^+ + S_{\text{turb}}^+$ (solid) as a function of inner height (a) and outer height (b). c-d) Normalized eddy viscosity ν_E (solid) plotted versus inner height (c) and outer height (d). (c) uses inner normalization; (d) uses normalization by $\nu\delta^+$ which approximately collapses data in the outer layer. Different colors are for different Reynolds numbers (cf. Tab. 1). Circles in (a) and (c) denote the height $z^- = 0.15$, diamonds in (b) and (d) are for $z^+ = 50$ as in Fig. 1

297 The viscous stress

$$S_{\text{visc}} = \nu \sqrt{\left(\frac{\partial U}{\partial z} \right)^2 + \left(\frac{\partial V}{\partial z} \right)^2} \quad (7a)$$

298 exhibits universal scaling when considered as $S_{\text{visc}}^+(z^+)$ (Fig. 2a); this normalization
 299 is also appropriate in the outer layer where the viscous stress is, however,
 300 small. Small deviations from the universal profile are observed for the smallest
 301 Reynolds number $\text{Re} = 500$; we attribute these to low-Re effects in the only trans-
 302 tionally turbulent flow ($\text{Re}_\tau = 479$). In contrast to the viscous stress, the total
 303 stress follows outer normalization, i.e. $S^+(z^-)$ is universal; a discrepancy in the
 304 inner layer does not occur as the total stress is approximately constant in the
 305 viscous and buffer layer, and a rescaling of the height would have no effect there;
 306 above, outer scaling is appropriate for the well-established dynamics in the over-
 307 lap region of inner and outer layer. This, however, implies a mixed scaling for the
 308 turbulent stress,

$$S_{\text{turb}} = \sqrt{\overline{u'w'}^2 + \overline{v'w'}^2}, \quad (7b)$$

309 where dashed quantities u' , v' , w' indicate deviations from the mean and the
 310 overbar denotes horizontal and time averaging. Indeed, S_{turb} only follows inner
 311 normalization below $z^+ \lesssim 20$ (where the turbulent contribution is negligible). In
 312 the outer layer, where $S_{\text{visc}} \rightarrow 0$, S_{turb}^+ follows outer normalization for $z^- \gtrsim 0.15$ —
 313 with increasing accuracy for larger Re and larger distance from the surface. In the
 314 overlap region, i.e. for $z^+ > 20$ and $z^- < 0.15$, the mixed scaling for the turbulent
 315 stress can be expressed as

$$S_{\text{turb}}^+(z^+, \text{Re}_\tau) = S^+(z^-) - S_{\text{visc}}^+(z^+), \quad (7c)$$

316 where $z^- = z^+/\text{Re}_\tau$.

317 The ~~Eddy-eddy~~ viscosity plays a crucial part when modelling profiles and
 318 the vertical transport in turbulent flow. In analogy to the Fick-law for molecular
 319 diffusion, the eddy diffusivity is the effective diffusivity that yields the turbulent
 320 transport S_{turb} based on the strain rate. For the ~~symmetries in the flow (horizontal~~
~~homogeneity, and assumptions of horizontal homogeneity and incompressibility~~
~~(which implies $W = 0$, i.e. no mean wall-normal velocity)~~, it is

$$\nu_E = \frac{S_{\text{turb}}}{\sqrt{\left(\frac{\partial U}{\partial z} \right)^2 + \left(\frac{\partial V}{\partial z} \right)^2}} = \nu \frac{S_{\text{turb}}}{S_{\text{visc}}}. \quad (8a)$$

323 The inner normalization of ν_E is obtained when dividing by the molecular viscosity:

$$\nu_E^+ = \nu_E / \nu = S_{\text{turb}} / S_{\text{visc}}. \quad (8b)$$

324 Under this normalization, the profiles of eddy viscosity collapse below $z^+ \approx 20$
 325 with a tendency towards better collapse at higher z^+ for higher Reynolds number
 326 (up to $z^+ \approx 50$ for $\text{Re} = 1600$; Fig. 2c). In the outer layer, the eddy viscosity
 327 is characterized by a distinct minimum at $z^- \approx 0.6 - 0.8$, and we find that the
 328 following mixed normalization of ν_E by the geostrophic wind and friction velocity
 329 collapses the value of ν_E at this minimum (cf. Fig. 2d):

$$\nu_E^- = \nu_E^+ \frac{1}{\delta^+} = \nu_E \frac{1}{\nu} \frac{\nu}{u_* \delta} = \nu_E \frac{f}{u_*^2}. \quad (8c)$$

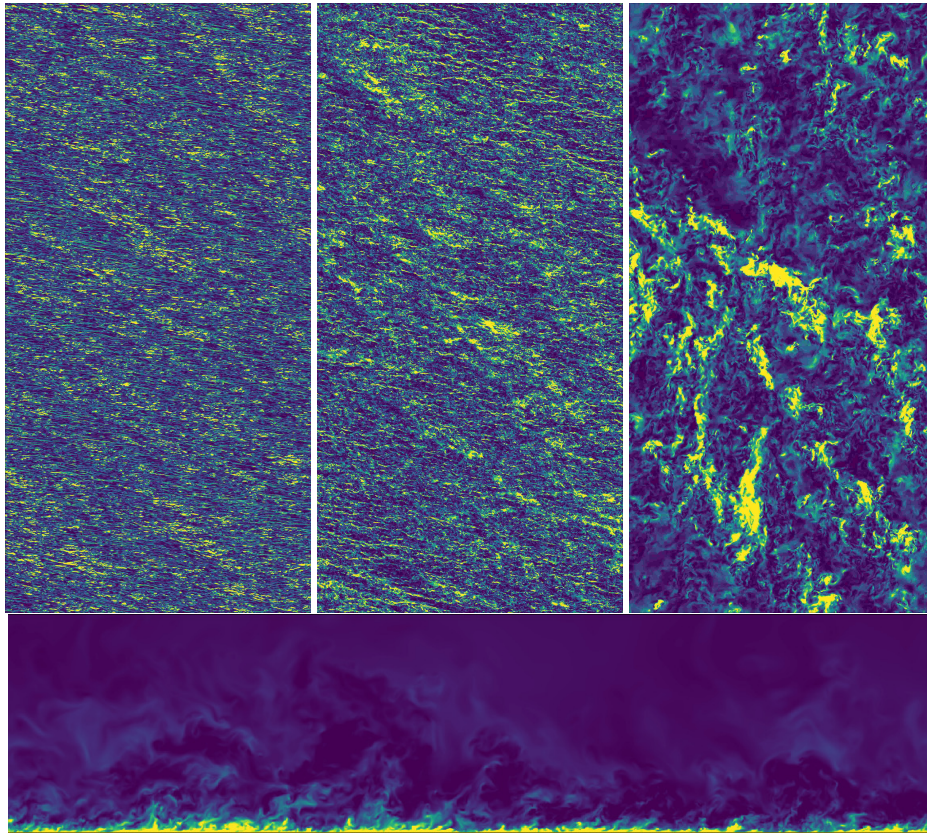


Fig. 3 Horizontal slices of turbulence kinetic energy in the Buffer layer ($i=10$, $y^+ \approx 10.5$), logarithmic Layer-layer ($i=100$, $y^+ \approx 150$), and outer layer ($i=400$, $y^+ \approx 1200$) of the case with $Re_\tau = 2978$; coloring between percentiles 4 and 96 of the respective image. Lower panel: streamwise–vertical intersect through the domain

330 Substantial variation of the profiles is, however observed below and above this
 331 minimum for different Re which illustrates that this normalization is probably not
 332 generally appropriate across the outer layer.

333 The organization of the flow with $Re_\tau = 2978$ is depicted in terms of the
 334 turbulence kinetic energy in Fig. 3. In vicinity of the wall, at $y^+ \approx 10$, (Fig. 3a),
 335 elongated streaks aligned with the surface shear stress dominate. Moving away
 336 from the wall, to $y^+ \approx 150$ (well within the logarithmic region), the structures are
 337 larger and more isotropic, but they are still largely aligned with the surface shear
 338 stress. In the upper part of the outer layer, around $y^+ \approx 1000$, no clear signature of
 339 the surface veering direction is found, and intense TKE structures (bright yellow)
 340 are organized on a large spatial scale with weaker eddies (greenish structures) and
 341 quiescent regions in between.

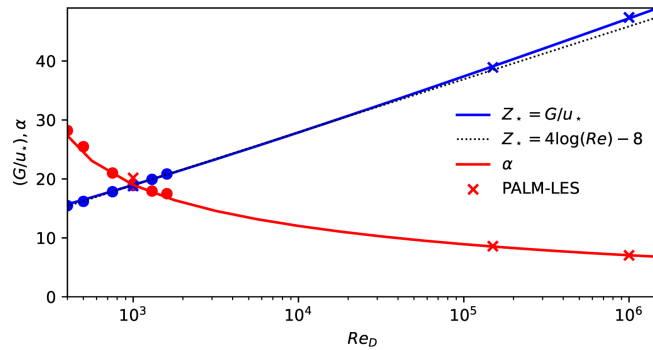


Fig. 4 Variation of geostrophic drag, Z_* , and surface veering, α_* , with Reynolds number according to the theory by Spalart et al. (1989) and as estimated from DNS data

342 **4 A universal Reynolds-number-independent velocity profile for the**
 343 **turbulent Ekman layer**

344 We now turn to the formulation of a general velocity profile that is fully determined
 345 by the only parameter of the idealized problem, namely a Reynolds number repre-
 346 senting the scale separation or geometric size of the problem. This precludes, first,
 347 a drag law wherewith we begin this section (4.1). Based on the scaling arguments
 348 put forward in Sec. 3, we then develop, second, a formulation of the wind vector
 349 in the Ekman layer (Sec 4.2). Finally, we come up with a separate formulation of
 350 the, third, stream-wise and, fourth, span-wise velocity components in the overlap
 351 and inner regions of the flow.

352 **4.1 Drag-law**

353 A drag-law for Ekman flow determines—as a function of Reynolds number alone—the
 354 surface drag. This can be formulated by the normalized surface friction, u_*
 355 (Eq. (1b), also termed geostrophic drag), and the direction of surface shear stress,
 356 α_* (Eq. (1c), also termed wind veer). A non-zero veering of the wind is a rather
 357 special case in comparison with most turbulent flows considered in an engineering
 358 context, and it confronts us with a situation where the most appropriate coordinate
 359 system for analysis (namely that aligned with the surface shear stress) is a priori
 360 unknown. We compare our DNS data against a semi-empirical drag-law based on
 361 integral consideration (Spalart 1989) and find, as demonstrated in previous work
 362 (Ansorge and Mellado 2014), excellent agreement in the range $400 < \text{Re} < 1600$,
 363 representing a factor of 16 in variation of viscosity.

364 We also find that the solution of the transient equation involved in estima-
 365 tion of u_* for a given Reynolds number Re_D is approximated reasonably by the
 366 formulation

$$Z_* = 4 \log(\text{Re}_D) - 8 \quad (9)$$

367 which quantifies the ‘weak’ dependence of u_* on the Reynolds number as an ap-
 368 proximately logarithmic one, at least for problems with a scale separation on the
 369 order that is relevant to geophysical problems ($Re_D < 10^8$).

370 4.2 Profile in the Ekman layer

371 Formulations for the outer layer that take into account the rotation (and thus
 372 deviation from the channel-flow analogy) need to be matched to the framework of
 373 surface similarity. A smooth transition from the inner layer to the Ekman layer,
 374 where the wind is characterized by a turning of its mean direction, is not eas-
 375 ily achieved. Optis et al. (2014), for instance, define an “*effective geostrophic wind*
 376 *vector that has the same magnitude of the observed surface geostrophic wind and is ro-*
 377 *tated by the angle α [their nomenclature]*” to overcome the unsteady transition when
 378 approaching the Ekman layer from below. Such rotation of the wind vector is *a*
 379 *posteriori* justified by the observational data that the model outcomes are com-
 380 pared to. This need for a connection of the two reference frames is a manifestation
 381 of a mismatch in the theoretical treatment of the inner and outer layer in this
 382 rotating flow configuration.

383 The text-book solution for Ekman flow makes use of the physical boundary
 384 conditions (BCs) for the ABL (no-slip at the bottom and geostrophic wind in the
 385 free atmosphere) and a constant eddy viscosity. Specifying the boundary conditions
 386 at top and bottom eliminates one mode of the analytical solution, and it determines
 387 the magnitude of the spiral. In doing so, one has to assume that the solution is
 388 appropriate across the entire ABL, which is not the case: The dynamics put forth
 389 by Ekman in 1905 are not appropriate in the surface layer of the ABL; better
 390 approximations exist for the logarithmic, buffer, and viscous sublayers. In view of
 391 this situation, we use an adapted Ekman spiral that does not enforce the boundary
 392 conditions at the surface but at a different height while maintaining the restriction
 393 to constant eddy viscosity. This is achieved by considering the Ekman spiral only in
 394 the Ekman layer, thus giving way for the well-established logarithmic and viscous-
 395 layer profiles in the lower surface layer. Based on the derivation in App. A.1, this
 396 profile is given by

$$\frac{1}{G} \begin{pmatrix} U_{ek} \\ V_{ek} \end{pmatrix} = \begin{pmatrix} 1 \\ 0 \end{pmatrix} + e^{-z_{ek}} \left[a_{ek} \begin{pmatrix} -\cos z_{ek} \\ \sin z_{ek} \end{pmatrix} + b_{ek} \begin{pmatrix} \sin z_{ek} \\ \cos z_{ek} \end{pmatrix} \right]. \quad (10a)$$

397 with $z_{ek} = \delta_{ek}(z - s_{ek})$. The right-hand-side consists of two modes with magnitude
 398 a_{ek} and b_{ek} shifted by $\pi/2$ with respect to each other. In the classic case, the second
 399 mode governed by b_{ek} is incompatible with the surface boundary condition. While
 400 this is not the case here for the general form of the profile, the phase shifts can also
 401 be captured by the parameter s_{ek} , and we stick with to a single-modal approach,
 402 i.e., we let $b_{ek} = 0$.

403 This single-modal solution is characterized by three parameters, (i) an Ekman-
 404 layer depth scale δ_{ek} , (ii) the magnitude parameter of the spiral a_{ek} , and (iii) a
 405 zero-crossing point for the velocity s_{ek} . The effects of varying these parameters
 406 are illustrated in Fig. 5 where the classic Ekman solution is recovered by setting
 407 $a_{ek} = 1$, $s_{ek} = 0$ and $\delta_{ek} = \sqrt{2\nu/f}$. These parameters are *a priori* unknown as
 408 they need to conform to the turbulent state of the boundary layer; we use our
 409 DNS data to arrive at best estimates for them.

410 **The Ekman-layer depth scale δ_{ek}** is fundamentally defined by the eddy vis-
 411 cosity. However, we have seen in Section 3 that a characteristic value for the
 412 eddy diffusivity is not easily obtained for its strong dependence on the Reynolds
 413 number and distance from the surface. We therefore resort to the physical man-
 414 ifestation of the eddy diffusivity in an Ekman layer, and use the boundary layer

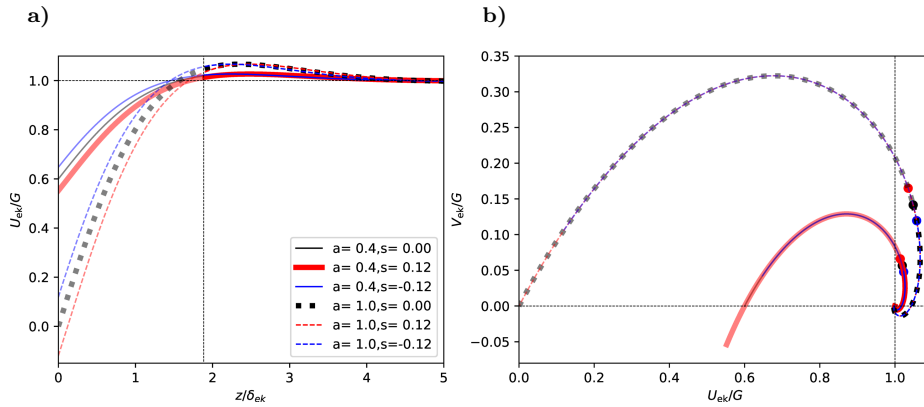


Fig. 5 a) Generalized Ekman-profile of the geostrophic-aligned component U_{ek} . b) Hodograph for the geostrophic-aligned and pressure-gradient aligned components U_{ek} and V_{ek} . Thick, black dashed line shows the classic solution. The height corresponding to $z^- = 0.30$ is marked by the dashed line in panel (a) and by filled circles in panel (b). The hodograph and profiles above this reference height are shown as solid lines, below as opaque line.

415 depth $\delta_{\text{ek}} = 0.66\delta \times 2\pi$. For the relation $\delta_{\text{ek}} = \sqrt{2\nu_{\text{ek}}/f}$, this yields $\nu_{\text{ek}} \propto u_*^2/f$ in
416 accordance with the observations in Sec. 3 (Eq. 8c).

417 **The magnitude parameter of the Ekman spiral**, a_{ek} , defines the super-
418 geostrophic maximum of the wind profile aloft the logarithmic layer. Our sim-
419 ulations suggest this maximum of the velocity deficit remains constant when nor-
420 malized by u_* as shown in Fig. 6. The numerical value of a_{ek} is estimated from
421 visual comparison, and we find $a_{\text{ek}} = 8.4u_*$; while this appears rather large, it is
422 pre-multiplied by $e^{-z_{\text{ek}}}$ which has already decreased to $\mathcal{O}(0.1)$ at the height of this
423 maximum. This choice ascertains that the velocity deficits $U/u_* - Z_*$ and $V/u_* - Z_*$
424 do not depend on the velocity scale u_* , but only on G as

$$U_{\text{ek}}/u_* - Z_* \propto a_{\text{ek}}Z_* = 8.4G. \quad (11)$$

425 **The offset parameter** s_{ek} defines the zero-crossing height of the profile (in
426 contrast to δ_{ek} , which determines the thickness across which the wind veering
427 takes place). Physically, this offset can be understood as the height at which the
428 surface was located assuming a perfect Ekman flow down to the surface. As this
429 is not the case, and gradients are steeper in the highly turbulent boundary layer
430 flow encountered when approaching the surface, the offset is smaller than zero (the
431 fully turbulent boundary layer is actually thinner than an Ekman layer would be).
432 From our DNS data, we estimate $s_{\text{ek}} = -0.12$.

433 In summary, the outer layer of Ekman flow is characterized by a turning of
434 the wind velocity and the super-geostrophic maximum that is sustained by mo-
435 mentum convergence at the inflection point of the velocity profile. The super-
436 geostrophic maximum of streamwise velocity and a secondary minimum aloft the
437 bulk-turbulent part of the boundary layer are well-described by a classic Ekman
438 spiral with adapted boundary conditions and a shift in reference height. Corre-
439 sponding profiles are shown in comparison with data from three DNS runs in
440 Fig. 6. The idealized profiles capture the secondary minimum and convergence to
441 the geostrophic equilibrium in the non-turbulent flow very well.

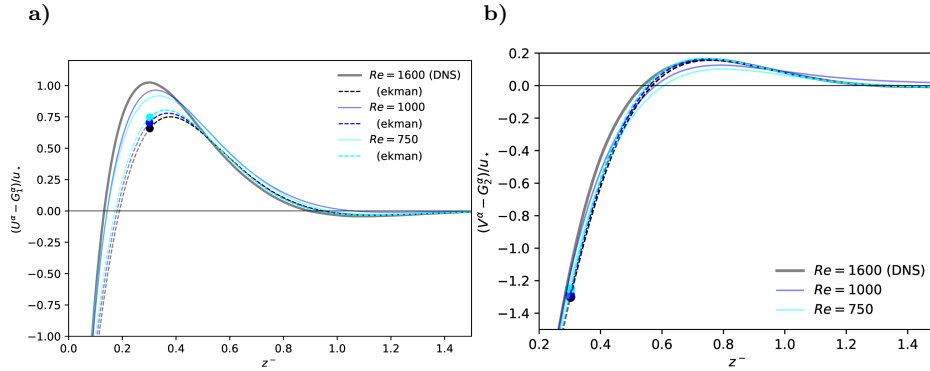


Fig. 6 Shear-aligned velocity deficit for the streamwise (panel **(a)**) and spanwise (panel **(b)**) components of the mean velocity U^α and V^α . Solid lines show DNS data, dashed lines the Ekman profiles U_{ek} and V_{ek} as defined in Eq. 10. Variations in U_{ek} and V_{ek} are a consequence of the normalization and related to changes in u_* and α_* among the different Re_D .

442 4.3 Streamwise velocity component

443 Well-established theories exist for the streamwise velocity profile, which in non-
 444 rotating flows is aligned with the surface shear stress due to the geometry. These
 445 theories cover various regimes based on their distance from the wall and the relative
 446 influence of viscosity, turbulence, and interaction with the outer flow region, with
 447 the logarithmic law for the mean velocity serving as a central reference point.

448 In immediate vicinity to the surface, local turbulent mixing cannot occur for
 449 the no-slip/no-penetration boundary condition, and the mean velocity is described
 450 by a viscous profile of the form

$$U^{\alpha_*+} = z^+ \quad (12a)$$

451 where the direction of the velocity points into the exact opposite direction of the
 452 wall shear stress τ . In absence of roughness elements and for small roughness
 453 ($z_0^+ < 5$), this linear regime is known as viscous sub-layer Foken (2002); Foken
 454 et al. (1978). In fact, this law of the wall has no degree of freedom given the
 455 drag, i.e. once u_* and α_* are defined. However, theoretical foundation is lacking
 456 for the exact shape of the velocity profile in the buffer layer; though crucial for
 457 turbulence production, it is commonly understood as a transition region between
 458 the linear profile at the surface and the logarithmic profile aloft. A pure blending
 459 from the linear velocity profile into the logarithmic one is, however, not reasonable
 460 as both the linear and logarithmic profile overestimate the velocity in the buffer
 461 layer. We therefore introduce a two-step correction procedure, accounting for the
 462 smaller-than linear growth beyond $z^+ \approx 5$, and assuring smooth matching with
 463 the logarithmic law at $z^+ = 40$:

$$U_{\text{inner}}^{\alpha_*+} = \frac{z^+}{1 + c_1(y^+)^2} + (c_2 z^+ - a_{\text{match}}) \frac{1 + \tanh[0.2(z^+ - 22)]}{2} + c_3 e^{-c_4(z^+ - 22)^2}. \quad (12b)$$

464 We use here

$$c_1 = 0.00185; \quad c_2 = 0.195; \quad c_3 = 0.4; \quad c_4 = 0.35.$$

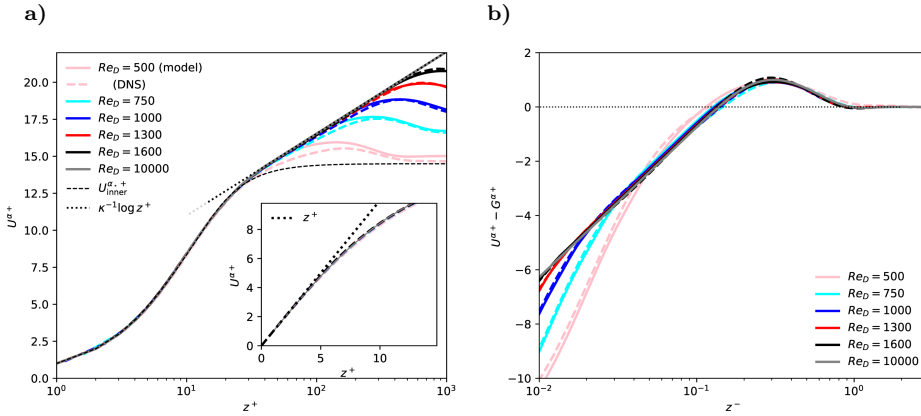


Fig. 7 Shear-aligned profiles of velocity components $U^{\alpha*+}$ in inner (left) and outer (right) units.

465 The second and third terms on the right hand side vanish for $z^+ \ll 22$, and
 466 $c_1 = 0.00185$ implies an approximately 5% correction at $z^+ = 5$ and an 18.5%
 467 correction at $z^+ = 10$. The second and third term on the R.H.S. of eq. (12b) are
 468 an empirical fit to the velocity profiles observed in the buffer layer and appear
 469 independent of the Reynolds number for the range observed here. The coefficient
 470 a_{match} , which has no effect in the viscous sublayer, is then used to match this
 471 formulation to the logarithmic law employed above.

472 In the logarithmic region, we use the profile

$$U_{\log}^{\alpha*+} = \frac{1}{\kappa} \log z^+ + C \quad (12c)$$

473 with the von-Kármán constant $\kappa = 0.416$ and the boundary condition $C = 5.4605$.
 474 For this logarithmic law, $a_{\text{match}} = 3.569861$ for a matching at $z^+ = 40$.

475 4.4 Spanwise velocity component

476 The background rotation and associated veering of the surface wind implies a
 477 non-zero profile for the span-wise velocity which challenges the conventional as-
 478 sumptions related to the channel-flow analogy: While the analogy with channel
 479 flow in vicinity of the wall implies that the streamwise component be zero or at
 480 least small, the veering requires a value of $V_{top} = U_G \sin \alpha_*$ in the free stream (and
 481 thus also at the top of the boundary layer if we assume that any substantial veloc-
 482 ity gradient is confined to the turbulent part of the flow). This continuous rotation
 483 of the wind vector is conveniently visualized by velocity hodographs aligned with
 484 the outer, geostrophic flow (cf. Fig. 5b) and normalized by the geostrophic wind.
 485 The geometry of the flow and its drag imply the following for any hodograph: (i)
 486 the boundary conditions at the surface, (ii) the boundary condition at the top,

⁴⁸⁷ and (iii) the inclination of the hodograph at the origin by the surface veering:

$$V^{\alpha_*}(z = 0) = 0, \quad (13a)$$

$$\lim_{z \rightarrow \infty} V^{\alpha_*} = G \sin \alpha_*, \quad (13b)$$

$$\partial_{z+} V^{\alpha_*+}|_{z=0} = 0. \quad (13c)$$

⁴⁸⁸ Outer scaling of the velocity profile further implies that the velocity deficit
⁴⁸⁹ of $(V^{\alpha_*} - G^{\alpha_*})/u_*$ be a universal function of the outer height z^- . In the outer
⁴⁹⁰ region of the flow (for $z^- \mapsto 1$), $f_V(z^-)$, should govern the spanwise velocity
⁴⁹¹ profile, as is supported by our DNS data (Fig.1b); above $z^- \approx 0.3$, this profile is
⁴⁹² very well approximated by the Ekman-turning derived above (Eq. (10); Fig. 6b).
⁴⁹³ While this deficit is a signature of outer rotation, it is inappropriate to extend this
⁴⁹⁴ general relation to the surface where inner scales matter: On the one hand, the
⁴⁹⁵ variation of the spanwise velocity deficit across the boundary layer (i.e. between
⁴⁹⁶ $0 < z^- < 1$) must match the difference implied by the drag law (u_*, α_*) and the
⁴⁹⁷ constant value of V^{α_*} around $z^- = 0.3$. On the other hand, provided the outer
⁴⁹⁸ velocity deficit is Re independent—the Re-dependence of α_* and u_* implies that
⁴⁹⁹ this difference cannot be constant as a function of Re. We hence ask, how does the
⁵⁰⁰ span-wise component scale when the surface is approached? Clearly, the spanwise
⁵⁰¹ contribution is small in comparison with the streamwise component throughout
⁵⁰² much of the layer below $z^- \approx 0.3$. However, we cannot assume $V = 0$ if a smooth
⁵⁰³ matching between the inner and outer layers shall be achieved. In this context, we
⁵⁰⁴ first realize that the velocity deficit $(V^{\alpha_*} - G^{\alpha_*})/u_*$ approaches a Re-independent
⁵⁰⁵ constant around $C_{V0} = Z_* \sin \alpha = 6.1$ at the surface; deviations from this constant
⁵⁰⁶ are only found for the lowest Reynolds numbers which is in accordance with the
⁵⁰⁷ low-Re correction suggested by Spalart (1989). This constrains the wind veer, and
⁵⁰⁸ it quantitatively shows that the decreasing wall friction manifest in an increase of
⁵⁰⁹ Z_* exactly compensates the decrease of wind turning measured by $\sin \alpha_*$.

⁵¹⁰ If the difference across the boundary layer is constant (C_{V0}) vs. Re, the av-
⁵¹¹ eraged gradient $\partial_{z+} V^{\alpha_*+}$ of the spanwise velocity component must decrease as
⁵¹² $1/\delta^+$ with increasing Re_τ . Hence, it should—at a fixed height—be $V^{\alpha_*} \propto (\delta^+)^{-1}$. A
⁵¹³ profile that agrees with the constraints of the profile at the surface and exploits
⁵¹⁴ the dependence of V^{α_*} on δ^+ is

$$V^{\alpha_*} \frac{\delta^+}{G} = f_{V,\text{visc}}(z^+) = v_{\text{ref}} (\omega_v z^+ - 1 + \exp[-\omega_v z^+]), \quad (14)$$

⁵¹⁵ where v_{ref} controls the magnitude of the profile and ω_v sets the height at which the
⁵¹⁶ profile transitions into an approximately linear one. We find excellent agreement
⁵¹⁷ with the DNS data for $500 \leq \text{Re}_D \leq 1600$ below $z^+ \approx 15$ with

$$v_{\text{ref}} = 18.85; \quad \omega_v = 0.2353$$

⁵¹⁸ (cf. Fig. 8b).

⁵¹⁹ For the adjacent surface layer, we find a log-like transition from the quasi-linear
⁵²⁰ profile inner profile around $z^+ = 10$ to a linear profile with increasing Re (Fig. 8b).
⁵²¹ We model this transition by

$$f_{V,\log}(z^+) = \frac{V_{\log}(z^+)}{G} \delta^+ = a_{\log} + b_{\log} \log z^+ + c_{\log} z^+. \quad (15)$$

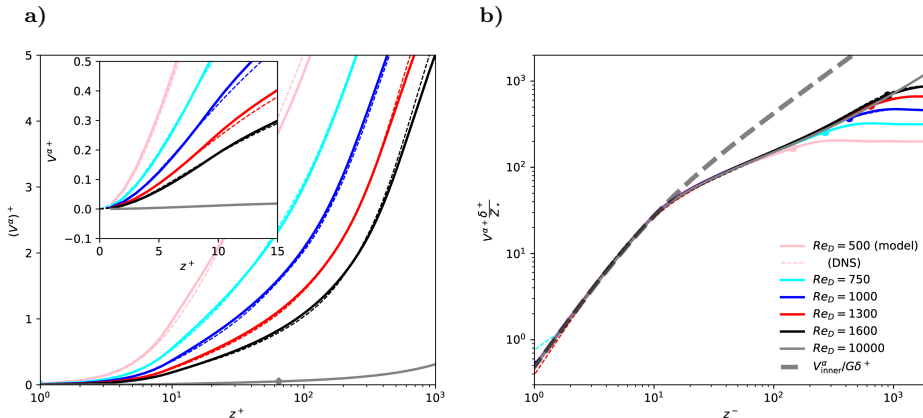


Fig. 8 Profiles of shear-aligned span-wise velocity $(V^\alpha)^+$ versus inner height. Dashed lines show DNS data, thick, opaque lines are from the semi-empirical theory developed above. Panel (a) shows standard inner normalization, panel (b) the inviscid normalization yielding a universal profile for the spanwise component of velocity in the inner layer.

522 This surface-layer profile matches the inner (viscous) scaling in vicinity of the
523 surface to the outer (Ekman) scaling above $z^- = 0.3$ when constrained by the
524 viscous profile at the bottom and the Ekman profile at the top:

$$f_{V,\log}(z^+ = 10) = f_{V,\text{visc}}(z^+ = 10) =: v_{10} \simeq 27.3 \quad (16a)$$

$$\frac{\partial}{\partial z^+} [f_{V,\log}]_{z^+ = 10} = \frac{\partial}{\partial z^+} [f_{V,\text{visc}}]_{z^+ = 10} =: d_{10} \simeq 4.01 \quad (16b)$$

$$f_{V,\log}(z^+ = 0.3\delta^+) = V_{\text{ek}}^{\alpha*}(z^- = 0.3)\delta^+ =: v_{03} \quad (16c)$$

525 where v_{03} is determined by $V_{\text{ek}}(0.3)$ and $U_{\text{ek}}(0.3)$ and depends on Re . Given the
526 Ekman formulation of the velocity profile introduced in Sec. 4.2, one may express
527 v_{03} using the Ekman profile introduced in Sec. 4.2 together with the approximation
528 for $u_*(\text{Re})$ found in Eq. (9). While the Re -dependency of a_{\log} , b_{\log} , c_{\log} is small,
529 it shows up in Fig. 1 where the normalized profiles of spanwise velocity become
530 more convex with increasing Re . We can now quantify this effect by means of the
531 change of c_{\log} versus Re which is shown in Fig. 9 (cf. Appendix A.2; a_{\log} and b_{\log}
532 are then determined by the universal values of v_{10} and d_{10}).

533 4.5 Matching of the inner and outer layer profiles

534 The formulations introduced above are continuous across the transition from the
535 inner to the outer layer. However, the requirement of smooth derivatives would
536 over-constrain the velocity profiles and is hence not applied. This can, in particular
537 for low or extremely high Re , cause discontinuity in the derivatives of the velocity
538 profiles around the transition from the inner to the outer layer. To avoid such
539 artificial discontinuity, the profiles are blended by an error-function transition
540 using a blending height $z_{\text{blend}}^- = 0.28 - 2.25\sqrt{1/\text{Re}_\tau}$ and a transition thickness

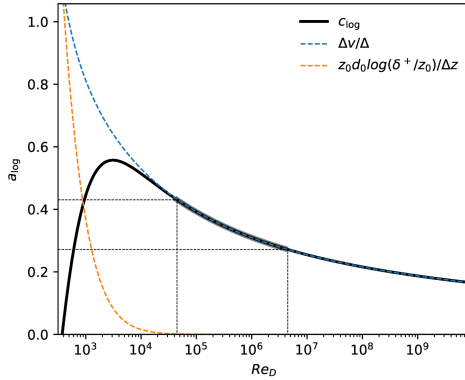


Fig. 9 Coefficients a_{\log} , b_{\log} and c_{\log} (cf. Eq. 15) as a function of the viscous Reynolds number Re_D . The approximate range of scale separation relevant for atmospheric application is found in between the dotted lines, where $a_{\log} \simeq 0$ and $c_{\log} \simeq 0.4$

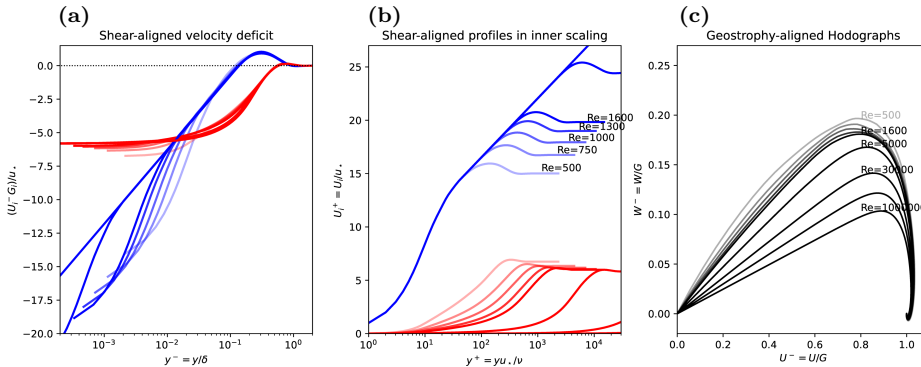


Fig. 10 (a) Velocity deficit, (b) velocity profile in shear-aligned hodographs and (c) hodograph in geostrophy-aligned coordinates. In panels (a) and (b), blue lines correspond to the streamwise component and red to the spanwise.

541 $z_{\text{trans}} = 2$, such that the weighting function $\omega(z^-)$ becomes

$$\omega(z^-) = \frac{1}{2} \left[\operatorname{erf} \left(z_{\text{trans}} \log \frac{z^-}{z_{\text{blend}}} \right) + 1 \right], \quad (17)$$

542 hence $u_{\text{total}} = (1 - \omega) \times u_{\text{inner}} + \omega \times u_{\text{outer}}$ and similar for v .

543 The resulting velocity profiles across the entire boundary layer are shown in
 544 inner and outer scaling as well as in hodograph- view in Fig. 10. The shear-aligned
 545 velocity deficit is shown in outer scaling highlighting the universality in the outer
 546 layer. The logarithmic scaling of the streamwise component is encountered as
 547 straight blue lines in panels (a) and (b) where the extent of the logarithmic range
 548 increases with Re towards lower values of z^- and higher values of z^+ depending
 549 on the scaling. Importantly, the logarithmic region is widening for increasing
 550 Reynolds number – irrespective of the scaling. In this simple inner scaling, the
 551 spanwise velocity (which follows a mixed scaling) does not collapse but seems to
 552 depend on Re (the collapse is seen in Fig. 8). However, the velocity deficit in outer
 553 units becomes approximately universal, also across the inner layer; this reflects

554 the compensation of reduced turning (α) by increased drag (u_*), and is consistent
 555 with the theoretical considerations discussed in 4.1.

556 The spanwise velocity at a fixed height scales approximately as Re_τ^{-1} (Sec. 4.4).
 557 However, the fraction of turning that is encountered within the inner layer of the
 558 flow amounts to about 1/3 of the total wind veer (Fig. 12a). This is because, in
 559 inner units, the inner layer grows as Re_τ which exactly compensates the reduced
 560 gradient of spanwise velocity. The hodographs show the well-known Ekman shape
 561 with the laminar profile as an outer limit and 'flatter' hodographs, corresponding
 562 to less turning, for increasing Reynolds number.

563 5 Discussion

564 5.1 Implications for surface-layer scaling

565 Eq. (14) establishes a **universal**-mixed scaling for the spanwise velocity in the vis-
 566 cous layer: While it requires the vertical coordinate to be expressed in inner units,
 567 the velocity itself is normalized by the geostrophic wind, and becomes inversely
 568 proportional to the friction Reynolds number $Re_\tau = \delta^+$ when considered at a fixed
 569 height. In vicinity of the surface, such mixed scaling has already been identified
 570 for higher-order statistics in convective flows (Mellado et al. 2016; Li et al. 2018),
 571 where large scales leave their signatures in vicinity of the surface. It is important
 572 to note here that, while V is a first-order statistic from a statistical perspective,
 573 the spanwise velocity is a higher-order correction term from the perspective of sim-
 574 ilarity theory and from the viewpoint of the channel-flow analogy that is routinely
 575 employed in the surface layer. Further, this is consistent with the scaling for the
 576 velocity hodograph found in Eq. (11) where the friction velocity also drops out.

577 In the surface layer, there is not only a mixed scaling—as we had already iden-
 578 tified in the viscous layer—but we cannot find a universal function onto which the
 579 profiles of spanwise velocity collapse. This additional degree of freedom reflects
 580 the inner–outer matching problem for the spanwise velocity. Rather than giving
 581 a **universal**-profile for this region, we resort here to a parametric description of
 582 the problem in terms of the function $f_{V,\log}$ determined by the parameters a_{\log} ,
 583 b_{\log} , c_{\log} which can be estimated based on the above scaling considerations for
 584 any Reynolds number. We note that, once the parameter a_{\log} is known, the pa-
 585 rameters b_{\log} and c_{\log} can be estimated solely based on $f_{V,\text{visc}}$, i.e. using the value
 586 v_{10} and d_{10} found for the viscous region of the flow. For the range of Reynolds
 587 number relevant to geophysical problems ($10^4 \lesssim Re_D \lesssim 10^6$), the variation of c_{\log}
 588 is, however, rather small.

589 5.2 Comparison with other theories

590 An alternative approach that considers viscous effects close to the surface is the
 591 van-Driest scaling (Van Driest 1956), where an exponential damping of Prandtl's
 592 mixing length is considered near the wall to yield

$$\frac{\partial u^+}{\partial z^+} = \frac{2}{1 + \sqrt{1 + (2\kappa z^+)^2 (1 - \exp[-z^+])}}; \quad (18)$$

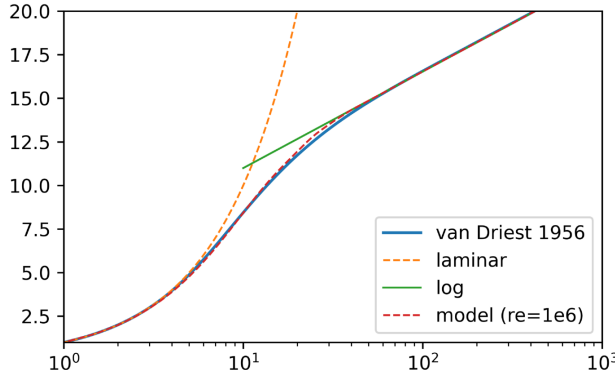


Fig. 11 Near-wall velocity profile according to the van-Driest scaling (blue, solid) in comparison with the present model (red, dashed), the viscous law of the wall (orange dashed), and the logarithmic law (green, solid)

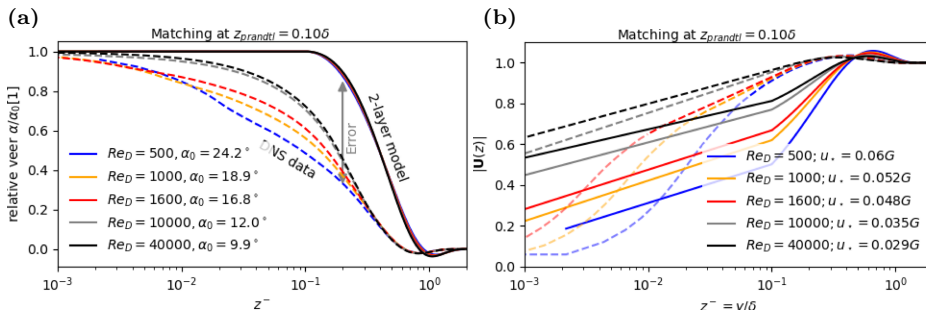


Fig. 12 Comparison of the DNS data (dashed lines) with the two-layer model proposed by Etling (solid lines) for different Reynolds number. Left panel shows the relative wind veer, right panel shows the velocity magnitude. The Etling model is calibrated by the surface veer from the DNS and the roughness parameter is chosen according to the correction factor $\exp \kappa A$ such that the total veer and velocity magnitude agree. Profiles in the buffer layer, defined here as $z^+ < 30$ are shown as opaque dashed lines as the two-layer model does not consider viscous effects.

593 the spanwise component is zero as no rotational effects are considered. Comparing
594 our proposed formulation for the stream-wise velocity in the inner layer to
595 Van Driest's formulation yields later convergence of the velocity onto the logarithmic
596 profile while, over all, it serves as an excellent model of the streamwise velocity
597 component (Fig. 11): Notable deviations (on the order of few percent) only occur
598 in the region $10 < z^+ < 30$, where the velocity transitions from the linear to the
599 logarithmic profile.

600 For the higher layers of the ABL, the Ekman spiral is the simplest model available.
601 When employed across the entirety of the ABL, the spiral of a turbulent
602 Ekman layer is flattened with respect to Ekman's laminar solution, which corre-
603 sponds to a reduction of the veering angle both at the surface and throughout the
604 ABL. We, however, find that a modified version of the Ekman spiral explicitly tak-
605 ing into account the surface boundary condition, is a consistent model and yields
606 excellent agreement with the velocity profiles from DNS (Sec. 4.2).

607 A two-layer model consolidating both the logarithmic and Ekman layer can
 608 be obtained following the arguments by Etling (2008), cf. Emeis (2018). Given
 609 a surface veering and a matching height (extent of the logarithmic layer), a for-
 610 mulation for the velocity profile across both the logarithmic and the outer layer
 611 is obtained. A comparison using the surface veering based on our model and a
 612 matching height of $z_{\text{prandtl}} = 0.05\delta$, which gives better results than the match-
 613 ing height of 0.1δ suggested by Etling (2008), is shown in Fig. 12. The overall
 614 shape of velocity magnitude is matched apart from the viscous and buffer layer
 615 (cf. Fig. 12b) that is neglected by the two-layer model. However, quantitative de-
 616 partures on the order of 10% occur across the inner layer: it turns out that the
 617 non-rotating profile, of the two-layer model in the logarithmic region yields too
 618 low overall velocity as the spanwise component contributes to the velocity across
 619 the inner layer. Deviations also occur with respect to wind direction; despite the
 620 rather low matching height, a substantial fraction of the rotation occurs within
 621 the lower part of the ABL and about 20% of the wind veer is not captured by the
 622 two-layer model. As the overall veer is given, the non-captured veer close to the
 623 surface is then compensated across the logarithmic layer. In the upper part of the
 624 boundary layer, both profiles match well.

625 The interpretation of flux and gradient profiles in terms of the K-theory (cf.
 626 Sec. 3, Fig. 2) suggests a certain universality in the inner layer, while a global
 627 collapse, i.e. across the boundary layer, is not obtained. While the K-Profiles con-
 628 cern the total stress, a consistent formulation of the turning would also require its
 629 partitioning to the individual components, i.e. the orientation of the stress vector
 630 $(\bar{u}'w', \bar{v}'w')$ in the horizontal plane. If K-theory shall be used, this stress vector
 631 needs to be anti-parallel to the corresponding stress vector $(\partial_z U, \partial_z V)$. Fig. 13
 632 shows the direction of the velocity, gradient and stress vectors across the bound-
 633 ary layer. It turns out that the negative stress vector with respect to the wind
 634 direction and the flux vectors (absolute) have an approximately similar direction.
 635 It appears that both rotate by about 270° ($3\pi/2$) across the boundary layer. Apart
 636 from the lower part of the Ekman layer ($0.2 < z^- < 0.7$), where there is a slight
 637 dependence on Re , the direction of stress appears to be universal, which is a
 638 consequence of the Ekman profile introduced in Sec. 4.2. However, this implies
 639 a misalignment between the flux and the stress on the order of the wind turn-
 640 ing, and indeed Fig. 13b shows a misalignment up to $\pi/8$. This is in accordance
 641 with the expectation by (Townsend 1976, Chap. 7.18) and prevents the transfer
 642 of energy from the mean flow to turbulence at these heights, thus preventing a
 643 boundary-layer growth. While the behavior in the inner layer seems to depend on
 644 Re , there emerges universality in the misalignment across the outer layer, suggest-
 645 ing that a consideration of misalignment in the context of K-theory is possible
 646 when developing formulations for higher-order quantities.

647 6 Conclusions

648 We investigate the wind veer and fundamental scaling properties of the veloc-
 649 ity profiles in Ekman flow. Based on scaling considerations and direct numerical
 650 simulation spanning one decade in external separation from $Re_A = 1.25 \times 10^5$ to
 651 $Re_A = 1.28 \times 10^6$, we derive a ~~universal formulation for the closed formulation for~~
 652 both horizontal components of the velocity profile in a stationary, smooth Ekman

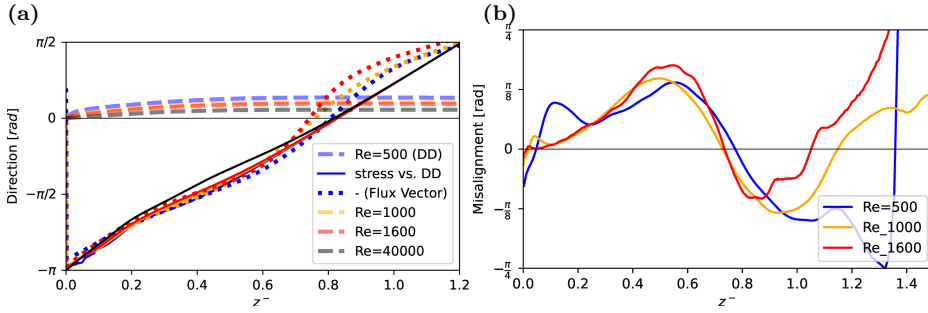


Fig. 13 Panel (a) shows the wind direction (DD) as thick dashed lines and the direction of stress relative to DD as thin solid lines, both according to our profile model. The direction of the negative flux vector ($\overline{u'w'}, \overline{v'w'}$) based on DNS data is shown as a dotted line. In panel (b), we plot the misalignment, i.e. the angle, between the flux vector and the shear vector, where the shear vector is defined accordingly as $(\partial_z U, \partial_z V)$.

layer. This formulation is consistent with the DNS data and also yields reasonable results at geophysical scale separation; the logarithmic law of the mean velocity is recovered with the well-known limits and deviations towards the surface and Ekman layer. The classic formulation of the Ekman layer, employing the surface boundary condition, is replaced by a modified solution that can be obtained by Ekman's system of governing equations, but using different boundary conditions that are more appropriate of the actual situation encountered in the planetary boundary layer. The three parameters that characterize this boundary condition are estimated based on DNS data.

To quantify the spanwise velocity component consistently across the boundary layer, we derive a universal scaling of the spanwise velocity component in a shear-aligned reference frame. For the *inner layer*, we find the mixed scaling

$$V^{\alpha_*}/G = \frac{1}{\delta^+} f(z^+) \quad (19)$$

that is, the spanwise velocity normalized by the outer velocity scale is a universal function of the inner height and Friction Reynolds number $Re_\tau = \delta^+$. This scaling is derived here based on scaling considerations, and it is in excellent agreement with the DNS data available. In the outer layer, the spanwise velocity follows outer scaling, consistently with the Ekman model discussed above (Sec. 4.2).

Our results suggest that there is no lower limit of the turning. Hence—despite its very large scale separation / huge Reynolds number—the ABL is not in the ‘limit’ of high Reynolds number from the perspective of wind veer, but always in a regime where changes in Re impact on the vertical partitioning of rotation.

674 A Appendices

675 A.1 Laminar Ekman solution with consideration of inner layer

676 The following Ekman system is obtained by averaging the Navier–Stokes equations horizontally
677 and over time and neglecting the turbulent transport terms (turbulence can then be considered

678 via the eddy-viscosity concept through variations in the viscosity ν):

$$\begin{pmatrix} \partial_t U \\ \partial_t V \end{pmatrix} = \begin{pmatrix} fV & +\nu\partial_z^2 U \\ -f(U-G) & +\nu\partial_z^2 V \end{pmatrix} \quad (20a)$$

$$\Rightarrow \partial_t(U+iV) = f(V-i(U-G)) + \nu\partial_z^2(U+iV) \quad (20b)$$

679 In stationary conditions, this system is solved by

$$\hat{u}(z) = U_\infty + e^{-\gamma z} [A \cos \gamma z + B \sin \gamma z] \quad (20c)$$

$$\hat{v}(z) = V_\infty + e^{-\gamma z} [-A \sin \gamma z + B \cos \gamma z] \quad (20d)$$

680 where the constants U_∞ , V_∞ set the top boundary condition and A and B set the bottom
681 boundary condition. The most common boundary condition for a surface Ekman layer is $A =$
682 $U_\infty = G$, $B = 0$, and $V_\infty = 0$. The lower boundary condition, however, neglects the existence
683 of the surface layer, and it appears reasonable to define $A = cG$ where $c < 1$ is a constant that
684 incorporates the increased shear in the surface layer. Given a 'matching height' z_{match} and
685 normalized matching height $\xi = \gamma z_{match}$ in the upper part of the inner layer, we can match
686 the Ekman profile to the inner layer by letting

$$\begin{aligned} u(z_{match}) &\equiv u_{match} = U_\infty + e^{-\xi} [A \cos \xi + B \sin \xi] \\ v(z_{match}) &\equiv v_{match} = V_\infty + e^{-\xi} [-A \sin \xi + B \cos \xi] \end{aligned} \quad (21a)$$

$$\Rightarrow \begin{pmatrix} u_{match} - U_\infty \\ v_{match} - V_\infty \end{pmatrix} = e^{-\xi} \begin{pmatrix} A \\ B \end{pmatrix} \begin{pmatrix} \cos \xi & +\sin \xi \\ -\sin \xi & +\cos \xi \end{pmatrix} \quad (21b)$$

$$(21c)$$

688 Matching the profile at $\xi = 0$, one obtains $A = \Delta u_{match}$ and $B = -\Delta v_{match}$; and when the
689 direction Ox is aligned with the geostrophic wind, we obtain the textbook-case $A = |\mathbf{G}|$ and
690 $B = 0$.

691 Otherwise, choosing $B \neq 0$ allows to introduce a phase shift of the Ekman rotation with
692 respect to the decay of the wind spiral. However, in our context, the thickness and position of
693 the spiral can already be controlled by the eddy viscosity and an offset in ξ , here we let $B = 0$.

694 A.2 Matching the spanwise velocity profiles in the inner layer

695 The spanwise profile in vicinity of the surface is given by $V/G = f_{V,\text{visc}} \delta^+$ with

$$f_{V,\text{visc}} = v_{\text{ref}} (\omega_v z^+ - 1 + e^{-\omega_v z^+}) \quad (22a)$$

$$f_{V,\log} = a_{\log} + b_{\log} \log z^+ + c_{\log} z^+ \quad (22b)$$

696 Matching the profiles and gradient $z_0 = 10^+$ and the value at $z_1 = 0.3\delta^+$ yields

$$v_{\text{ref}} (\omega_v z_0 + e^{-\omega_v z_0}) = v_0 = a_{\log} + b_{\log} \log z_0 + c_{\log} z_0 \quad (23a)$$

$$v_1 = a_{\log} + b_{\log} \log z_1 + c_{\log} z_1 \quad (23b)$$

$$v_{\text{ref}} \omega_z (1 - e^{-\omega_z z_0}) = d_0 = \frac{b_{\log}}{z_{10}} + c_{\log} \quad (23c)$$

697 The gradient condition implies $b_{\log} = (d_0 - c_{\log}) z_0$, and yields

$$v_0 - z_0 d_0 \log z_0 = a_{\log} + c_{\log} (z_0 - z_0 \log z_0) \quad (24a)$$

$$v_1 - z_0 d_0 \log z_1 = a_{\log} + c_{\log} (z_1 - z_0 \log z_0) \quad (24b)$$

$$\Rightarrow c_{\log} = \frac{\Delta v - z_0 d_0 \log z_1 / z_0}{\Delta z} \quad (24c)$$

698 with $\Delta z = z_1 - z_0$ and $\Delta v = v_1 - v_0$. Then, the coefficient a_{\log} is estimated as

$$a_{\log} = v_0 - z_0 d_0 \log z_0 - \frac{\Delta v - z_0 d_0 \log z_1 / z_0}{\Delta z} [z_0 - z_0 \log z_0]. \quad (24d)$$

699 We note that $\log(z_1/z_0)/(z_1 - z_0) \rightarrow 0$ for large z_1 , and as $z_1 = 0.3\delta^+$, this implies that the
 700 second term in c_{\log} only plays a role at low and intermediate Re . Then, a_{\log} can be estimated
 701 as

$$a_{\log} \simeq v_0 - z_0 \left[d_0 \log z_0 - \frac{\Delta v}{\Delta z} (1 - \log z_0) \right] \quad (24e)$$

702 for large Re .

703 **Acknowledgements** Simulations were carried out on the German supercomputing systems
 704 **hawk** at Höchstleistungsrechenzentrum Stuttgart (Bundesprojekt 44187) and **jewels** at Gauss
 705 Centre for supercomputing, Forschungszentrum Jülich (Projects **hku24** and **stadit**). We extend
 706 our thanks to Sally Issa for valuable feedback on the manuscript.

707 Declarations

708 **Author contributions** CA conceived the study, acquired funding, performed the simulation,
 709 analysed and plotted the data for this work. CA and HW interpreted the data and compiled
 710 the manuscript.

711 **Funding** CA is funded by the European Commission's 7th Framework Programme through
 712 the ERC 2019 Starting Grant trainABL (ID 851374). HW is funded by the Ministry for Science
 713 and Culture of Lower Saxony (project *ZukunftsKonzept Windenergieforschung*). Open Access
 714 funding for this publication through the DEAL agreement.

715 **Data availability** The data is available in long-term repositories and indexed by DOIs as
 716 cited in the list of references. Further analysis tools and processed data can be made available
 717 upon direct request.

718 **Conflict of interest** The Authors declare no competing interest.

719 **Open access** This article is licensed under a Creative Commons Attribution 4.0 International
 720 License, which permits use, sharing, adaptation, distribution and reproduction in any medium
 721 or format, as long as you give appropriate credit to the original author(s) and the source,
 722 provide a link to the Creative Commons licence, and indicate if changes were made. To view
 723 a copy of this licence, visit <https://creativecommons.org/licenses/by/4.0/>.

724 References

- 725 Ansorge C (2019) Scale Dependence of Atmosphere–Surface Coupling Through Similarity The-
 726 ory. *Boundary-Layer Meteorol* 170(1):1–27, DOI 10.1007/s10546-018-0386-y
 727 Ansorge C (2024a) Direct numerical simulation of turbulent Ekman flow ($Re=0500$): DOI
 10.17169/refubium-42505. DOI 10.17169/refubium-42505
 728 Ansorge C (2024b) Direct numerical simulation of turbulent Ekman flow ($Re=1000$): DOI
 10.17169/refubium-42507. DOI 10.17169/refubium-42507
 729 Ansorge C (2024c) Direct numerical simulation of turbulent Ekman flow ($Re=1300$): DOI
 10.17169/refubium-42508. DOI 10.17169/refubium-42508
 730 Ansorge C (2024d) Direct numerical simulation of turbulent Ekman flow ($Re=1600$): DOI
 10.17169/refubium-42509. DOI 10.17169/refubium-42509
 731 Ansorge C, Mellado JP (2014) Global Intermittency and Collapsing Turbulence in the Strat-
 732 ified Planetary Boundary Layer. *Boundary-Layer Meteorol* 153(1):89–116, DOI 10.1007/
 733 s10546-014-9941-3
 734 Ansorge C, Mellado JP (2016) Analyses of external and global intermittency in the logarithmic
 735 layer of Ekman flow. *J Fluid Mech* 805:611–635, DOI 10.1017/jfm.2016.534
 736 Baars WJ, Marusic I (2020) Data-driven decomposition of the streamwise turbulence kinetic
 737 energy in boundary layers. Part 2. Integrated energy and. *J Fluid Mech* 882:A26, DOI
 738 10.1017/jfm.2019.835

- 743 Barenblatt GI (1993) Scaling laws for fully developed turbulent shear flows. Part 1. Basic
744 hypotheses and analysis. *J Fluid Mech* 248:513–520, DOI 10.1017/S0022112093000874
- 745 Barenblatt GI, Goldenfeld N (1995) Does fully developed turbulence exist? Reynolds number
746 independence versus asymptotic covariance. *Phys Fluids* 7(12):3078–3082, DOI 10/bw2sq5
- 747 Blackadar AK, Tennekes H (1968) Asymptotic Similarity in Neutral Barotropic Plane-
748 tary Boundary Layers. *Journal of the Atmospheric Sciences* 25:1015–1020, DOI 10.1175/
749 1520-0469(1968)025<1015:ASINBP>2.0.CO;2
- 750 Brown AR, Beljaars ACM, Hersbach H, Hollingsworth A, Miller M, Vasiljevic D (2005) Wind
751 turning across the marine atmospheric boundary layer. *Quarterly Journal of the Royal*
752 *Meteorological Society* 131(607):1233–1250, DOI 10/dw2bxz
- 753 Calaf M, Meneveau C, Meyers J (2010) Large eddy simulation study of fully developed wind-
754 turbine array boundary layers. *Phys Fluids* 22(1):015,110, DOI 10/b7gc6v
- 755 Coleman GN, Ferziger JH, Spalart PR (1992) Direct Simulation of the Stably Stratified
756 Turbulent Ekman Layer. *Journal of Fluid Mechanics* 244:677–712, DOI 10.1017/
757 S0022112092003264
- 758 da Silva CB, Hunt JC, Eames I, Westerweel J (2014) Interfacial Layers Between Regions
759 of Different Turbulence Intensity. *Annu Rev Fluid Mech* 46(1):567–590, DOI 10.1146/
760 annurev-fluid-010313-141357
- 761 Dimotakis PE (2005) TURBULENT MIXING. *Annual Review of Fluid Mechanics* 37(1):329–
762 356, DOI 10.1146/annurev.fluid.36.050802.122015
- 763 Ekman VW (1905) On the influence of the earth's rotation on ocean currents. *Ark Mat Astron*
764 *Fys*, Vol 2 (1905), pp 1-53 2:1–53
- 765 Ellison TH (1955) The Ekman spiral. *Q J Roy Met Soc* 81(350):637–638, DOI 10.1002/qj.
766 49708135025
- 767 Emeis S (2018) Wind Energy Meteorology, 2nd edn. *Atmospheric Physics for Wind Power*
768 Generation, Springer, Heidelberg
- 769 Emeis S, Baumann-Stanzer K, Piringer M, Kallistratova M, Kouznetsov R, Yushkov V (2007)
770 Wind and turbulence in the urban boundary layer analysis from acoustic remote sensing
771 data and fit to analytical relations. *metz* 16(4):393–406, DOI 10.1127/0941-2948/2007/0217
- 772 Esau I (2004) Simulation of Ekman Boundary Layers by Large Eddy Model with Dynamic
773 Mixed Subfilter Closure. *Environmental Fluid Mechanics* 4(3):273–303, DOI 10/b8f3kh
- 774 Etling D (2002) Theoretische Meteorologie, 2nd edn. Eine Einführung, Springer-Verlag, Berlin,
775 Heidelberg
- 776 Etling D (2008) Theoretische Meteorologie: eine Einführung, 3rd edn. Springer, Berlin Heidel-
777 berg
- 778 Foken T (2002) Some aspects of the viscous sublayer. *metz* 11(4):267–272, DOI 10.1127/
779 0941-2948/2002/0011-0267
- 780 Foken Th, Kitajgorodskij SA, Kuznecov OA (1978) On the dynamics of the molecular tem-
781 perature boundary layer above the sea. *Boundary-Layer Meteorol* 15(3):289–300, DOI
782 10.1007/BF02652602
- 783 Ghannam K, Bou-Zeid E (2021) Baroclinicity and directional shear explain departures from
784 the logarithmic wind profile. *Quarterly Journal of the Royal Meteorological Society* 147:434–
785 464, DOI 10/gnj6z2
- 786 Gryning SE, Batchvarova E, Brümmer B, Jørgensen H, Larsen S (2007) On the extension of the
787 wind profile over homogeneous terrain beyond the surface boundary layer. *Boundary-Layer*
788 *Meteorol* 124(2):251–268, DOI 10.1007/s10546-007-9166-9
- 789 Höglström U (1988) Non-dimensional wind and temperature profiles in the atmospheric surface
790 layer: A re-evaluation. *Boundary-Layer Meteorology* 42:55–78, DOI 10.1007/BF00119875
- 791 Höglström U (1996) Review of some basic characteristics of the atmospheric surface layer.
792 *Boundary-Layer Meteorology* 78(3-4):215–246, DOI 10.1007/BF00120937
- 793 Jacobs AF, Van Boxel JH (1988) Changes of the displacement height and roughness length
794 of maize during a growing season. *Agricultural Forest Meteorol* 42(1):53–62, DOI 10.1016/
795 0168-1923(88)90066-4
- 796 Jiang Q, Wang S, Sullivan P (2018) Large-Eddy Simulation Study of Log Laws in a Neutral
797 Ekman Boundary Layer. *Journal of the Atmospheric Sciences* 75(6):1873–1889, DOI 10.
798 1175/JAS-D-17-0153.1
- 799 Jiménez J (2012) Cascades in Wall-Bounded Turbulence. *Ann Rev Fluid Mech* 44(Volume 44,
800 2012):27–45, DOI 10.1146/annurev-fluid-120710-101039
- 801 Kelly M, Gryning SE (2010) Long-Term Mean Wind Profiles Based on Similarity Theory.
802 *Boundary-Layer Meteorol* 136(3):377–390, DOI 10.1007/s10546-010-9509-9

- 803 Kelly M, Troen I (2016) Probabilistic stability and ‘tall’ wind profiles: Theory and method for
804 use in wind resource assessment. *Wind Energy* 19(2):227–241, DOI 10.1002/we.1829
- 805 Klein M, Maier RE, Schmidt H (2021) Stochastic modeling of transient neutral and stably-
806 stratified Ekman boundary layers. *P A M M* 21(1):e202100,146, DOI 10.1002/pamm.
807 202100146
- 808 Li Q, Gentine P, Mellado JP, McColl KA (2018) Implications of Nonlocal Transport and
809 Conditionally Averaged Statistics on Monin–Obukhov Similarity Theory and Townsend’s
810 Attached Eddy Hypothesis. *J Atmos Sci* 75(10):3403–3431, DOI 10.1175/JAS-D-17-0301.1
- 811 Lindvall J, Svensson G (2019) Wind turning in the atmospheric boundary layer over land. *Q
812 J Roy Met Soc* 145(724):3074–3088, DOI 10.1002/qj.3605
- 813 Mellado J, Ansorge C (2012) Factorization of the Fourier transform of the pressure-Poisson
814 equation using finite differences in colocated grids. *Z angew Math Mech* 92(5):380–392,
815 DOI 10.1002/zamm.201100078
- 816 Mellado JP, van Heerwaarden CC, Garcia JR (2016) Near-Surface Effects of Free Atmosphere
817 Stratification in Free Convection. *Boundary-Layer Meteorol* 159(1):69–95, DOI 10.1007/
818 s10546-015-0105-x
- 819 Mirocha JD, Churchfield MJ, Muñoz-Esparza D, Rai RK, Feng Y, Kosović B, Haupt SE,
820 Brown B, Ennis BL, Draxl C, Sanz Rodrigo J, Shaw WJ, Berg LK, Moriarty PJ, Linn RR,
821 Kotamarthi VR, Balakrishnan R, Cline JW, Robinson MC, Ananthan S (2018) Large-eddy
822 simulation sensitivities to variations of configuration and forcing parameters in canonical
823 boundary-layer flows for wind energy applications. *Wind Energy Science* 3(2):589–613, DOI
824 10/gn3nh4
- 825 Moin P, Mahesh K (1998) Direct numerical simulation: A tool in turbulence research. *Annual
826 Review of Fluid Mechanics* 30:539–578, DOI 10.1146/annurev.fluid.30.1.539
- 827 Momen M, Bou-Zeid E (2016) Large-Eddy Simulations and Damped-Oscillator Models of the
828 Unsteady Ekman Boundary Layer*. *Journal of the Atmospheric Sciences* 73(1):25–40, DOI
829 10.1175/JAS-D-15-0038.1
- 830 Momen M, Bou-Zeid E, Parlange MB, Giometto M (2018) Modulation of Mean Wind and
831 Turbulence in the Atmospheric Boundary Layer by Baroclinicity. *Journal of the Atmospheric
832 Sciences* 75(11):3797–3821, DOI 10/gfmn67
- 833 Monin AS (1970) The Atmospheric Boundary Layer. *Annual Review of Fluid Mechanics* 2:225–
834 250, DOI 10.1146/annurev.fl.02.010170.001301
- 835 Monin AS, Yaglom AM (1975) Statistical Fluid Mechanics, Vol. II, Dover Publications on
836 Physics, vol II. Dover Publications, Inc., Mineola
- 837 Optis M, Monahan A, Bosveld FC (2014) Moving Beyond Monin-Obukhov Similarity The-
838 ory in Modelling Wind-Speed Profiles in the Lower Atmospheric Boundary Layer un-
839 der Stable Stratification. *Boundary-Layer Meteorology* 153(3):497–514, DOI 10.1007/
840 s10546-014-9953-z
- 841 Rossby CG, Montgomery RB (1935) The layer of frictional influence in wind and ocean cur-
842 rents. *Papers in Physical Oceanography and Meteorology* III(3):1–101
- 843 Sakagami Y, Haas R, Passos JC (2020) Generalized Non-dimensional Wind and Temperature
844 Gradients in the Surface Layer. *Boundary-Layer Meteorol* 175(3):441–451, DOI 10.1007/
845 s10546-020-00510-3
- 846 Spalart PR (1989) Theoretical and numerical study of a three-dimensional turbulent boundary
847 layer. *J Fluid Mech* 205(-1):319, DOI 10.1017/S0022112089002053
- 848 Spalart PR, Coleman GN, Johnstone R (2008) Direct numerical simulation of the Ekman layer:
849 A step in Reynolds number, and cautious support for a log law with a shifted origin. *Phys
850 Fluids* 20(10):101,507, DOI 10.1063/1.3005858
- 851 Spalart PR, Coleman GN, Johnstone R (2009) Retraction: “Direct numerical simulation of the
852 Ekman layer: A step in Reynolds number, and cautious support for a log law with a shifted
853 origin” [Phys. Fluids 20, 101507 (2008)]. *Phys Fluids* 21(10):109,901, DOI 10.1063/1.3247176
- 854 Stoll R, Gibbs JA, Salesky ST, Anderson W, Calaf M (2020) Large-Eddy Simulation of the At-
855 mospheric Boundary Layer. *Boundary-Layer Meteorol* 177(2-3):541–581, DOI 10/gmbmzw
- 856 Svensson G, Holtslag AAM (2009) Analysis of Model Results for the Turning of the Wind
857 and Related Momentum Fluxes in the Stable Boundary Layer. *Boundary-Layer Meteorol*
858 132(2):261–277, DOI 10/bwknmt
- 859 Tennekes H (1973) A Model for the Dynamics of the Inversion Above a Convective Boundary
860 Layer. *Journal of the Atmospheric Sciences*
- 861 Townsend AA (1976) The Structure of Turbulent Shear Flow, 2nd edn. Cambridge University
862 Press

- 863 Van Driest ER (1956) On Turbulent Flow Near a Wall. *Journal of the Aeronautical Sciences*
864 23(11):1007–1011, DOI 10.2514/8.3713
865 Zikanov O, Slinn DN, Dhanak MR (2003) Large-eddy simulations of the wind-induced turbu-
866 lent Ekman layer. *J Fluid Mech* 495:343–368, DOI 10/ccbpbw